Economical Unsteady High-Fidelity Aerodynamics for Structural Optimization with a Flutter Constraint

Robert E. Bartels[1] and Bret K. Stanford[2]
NASA Langley Research Center, Hampton, VA, 23681

Structural optimization with a flutter constraint for a vehicle designed to fly in the transonic regime is a particularly difficult task. In this speed range, the flutter boundary is very sensitive to aerodynamic nonlinearities, typically requiring high-fidelity Navier-Stokes simulations. However, the repeated application of unsteady computational fluid dynamics to guide an aeroelastic optimization process is very computationally expensive. This expense has motivated the development of methods that incorporate aspects of the aerodynamic nonlinearity, classical tools of flutter analysis, and more recent methods of optimization. While it is possible to use doublet lattice method aerodynamics, this paper focuses on the use of an unsteady high-fidelity aerodynamic reduced order model combined with successive transformations that allows for an economical way of utilizing high-fidelity aerodynamics in the optimization process. This approach is applied to the common research model wing structural design. As might be expected, the high-fidelity aerodynamics produces a heavier wing than that optimized with doublet lattice aerodynamics. It is found that the optimized lower skin of the wing using high-fidelity aerodynamics differs significantly from that using doublet lattice aerodynamics.

Nomenclature

Variables

C	coefficient matrix of dimension $N \times N_e$
D	damping matrix
F	nodal force vector, N
g	generalized displacement vector, m
G	generalized force vector, N
$H(s)$	frequency domain aerodynamic influence coefficient (AIC) matrix of dimension $N \times N$, m
k	reduced frequency, $k = \omega L_R / U_\infty$
K	stiffness matrix, N/m
L_R	reference length
M	mass matrix, kg
N	number of node points
N_r	number of retained modes
N_e	number of modes in the expanded set, $N_e \geq N_r$
q_∞	dynamic pressure, N/m^2
$Q(s)$	frequency domain generalized aerodynamic influence coefficient (gAIC)

[1] Senior Aerospace Engineer, NASA Langley Research Center, MS 340, and AIAA Senior Member.
[2] Research Aerospace Engineer, NASA Langley Research Center, MS 340, and AIAA Senior Member.

	matrix of dimension $N_e \times N_e$, m
p	nondimensional Laplace variable, $p = sL_R/U_\infty$
s	dimensional Laplace variable, $s = \zeta\omega + i\omega$, s^{-1}
U_∞	freestream velocity, m/s
U_{EAS}	freestream equivalent air speed, m/s
x	vector of displacements, m
η	minimum modal flutter damping
λ_n	n^{th} chosen root in the Roger approximation of the generalized AIC matrix
ω	undamped natural frequency of structure, rad/sec
ω_f	frequency of flutter, rad/sec
Ω	diagonalized matrix of free vibration frequencies of the structure, rad/sec
ζ	true damping, $\zeta = 1/2\pi[ln(a_{n+1}/a_n)]$, where a_n is the n^{th} oscillation peak
Superscripts	
~	Laplace transform
$*$	chosen optimization constants
Subscripts	
b	baseline
m	modified

I. Introduction

Aeroelastic optimization of flexible wing structures typically seeks to minimize structural weight and/or fuel burn, with constraints placed upon various flight metrics. Of these constraints, the aeroelastic flutter margin is particularly critical, due to the abrupt, damaging, and sensitive nature of this failure mechanism, and also because a large fraction of the structural weight is typically allocated to satisfying the flutter constraint [1]. For transonic applications, the flutter boundary is very sensitive to aerodynamic nonlinearities, typically requiring high-fidelity Navier-Stokes simulations for its accurate prediction [2]. At the same time, flutter simulations based on computational fluid dynamics (CFD) are very computationally expensive, and somewhat incompatible to the high volume of function evaluations required for structural and aeroelastic optimization in an unsteady flowfield.

Aeroelastic optimization using Reynolds-averaged Navier-Stokes (RANS) CFD, nevertheless, is desirable since flowfield nonlinearity can have a significant effect on the optimized structure. With the progress in computing power, this approach to performing at least static aeroelastic optimization seems feasible for some cases, as attested to by recent published results [3–11]. In addition, there have been recent investigations into optimization of shape or aeroelastic properties using the adjoint method with the time-domain [12–15] or frequency-domain [16] Euler or Reynolds-averaged Navier-Stokes equations. In all of those time or frequency-domain studies, the configurations have either been two-dimensional or simple three-dimensional wings.

Given the complexity of industrial flight configurations and the growing recognition of the amount of grid resolution required for solution accuracy, flutter- or gust-based optimization of a structure (or of a coupled aerodynamics, structure and control system) driven by the unsteady Reynolds-averaged Navier-Stokes (URANS) equations, still seems to be years away from routine use. This limitation encourages finding other means to incorporate high-fidelity aerodynamics into a structural optimization when constrained by a required flutter onset margin.

Obviously, there has always been a motivation to understand and develop effective methods of including flutter constraints during structural optimization [17, 18]. Haftka and Yates [19] pioneered the development of a flutter constrained optimization method, using the low fidelity aerodynamic tools available at that time. More recent studies have addressed the problem of optimization with a flutter or gust load constraint [14, 20–26], but still used simplified

aerodynamics such as Euler CFD, doublet lattice, unsteady panel, or strip theory aerodynamics.

Linear unsteady aerodynamic tools exist that can compute an offline database of aerodynamic coefficients for a given planform [27–29]. As these coefficients are not functions of structural design variables, they may be used across the entire aeroelastic optimization process for an efficient handling of the flutter margin constraint. Linear flutter constraint boundaries are nonconservative (i.e., they overpredict the flutter dynamic pressure), and so a variety of tools exist to correct the unsteady aerodynamics, either based on CFD or wind tunnel data [30]. Overset-field panel methods have also been developed via oscillatory linearizations about a steady CFD result, interpolated onto a linear panel mesh [31]; the final result is a database of offline transonic aerodynamic coefficients, which as before, is highly amenable to aeroelastic optimization. Chen, et al. [32] have developed a method of transforming unsteady pressure coefficients from a baseline to a modified set of modes using a linearization of data from a nonlinear transonic small disturbance code.

In this paper, a somewhat simpler and possibly less expensive formulation than that in Ref. 32 is developed to transform unsteady aerodynamic data to an updated structural model. This method provides an economical way to generate a CFD-based flutter margin. The unsteady data is derived by using aeroelastic system identification tools [33] to output a generalized aerodynamic influence coefficient (gAIC) matrix. The Roger approximation [34] of either the URANS or doublet lattice method (DLM) aerodynamics are combined with the equations of structural dynamics to obtain flutter predictions at select Mach numbers. Ostensibly, the Roger approximation is only useful for the structure whose mode shapes (eigenvectors) were used for structural perturbations to generate the CFD-based unsteady aerodynamics. Methods exist, however, to project the Roger approximation terms from the baseline modal space into a modified modal space, making the technique well-suited for aeroelastic optimization, where the mode shapes will change from one design iteration to the next.

II. Aerodynamic Relationship between the Baseline and Modified Structures

The present goal is to drive a structural model from a baseline configuration toward a modified optimal structure under a flutter constraint utilizing CFD-based unsteady aerodynamics. It has been reported that under certain conditions the influence of the derivatives of the mode shapes on the generalized aerodynamic force is negligible. In this case, the terms carrying the influence of mode shape change on the gAIC can be neglected and the optimization is influenced mostly by natural frequency of the optimized structure [20, 22]. In the present case where high-fidelity CFD at transonic flight conditions is used, it is unclear whether the effect of a mode shape change on the gAIC will be insignificant. Thus, a more general approach is likely to be needed. In the approach used here, the high-fidelity unsteady aerodynamics of the baseline model is used to derive the gAIC matrix of the modified structure. This is done via a projection of the modified modes onto the baseline modal basis vectors.

Neglecting the structural damping, the equations of structural dynamics for the baseline structural model can be written

$$M_b\ddot{x} + K_b x = F_b \quad . \tag{1}$$

The unknown $x(t)$ is the vector of dynamic displacement increments and $F_b(t)$ is the vector of aerodynamic forcing increments at N node points, both from a steady-state equilibrium. A Laplace transformation yields

$$[s^2 M_b + K_b]\tilde{x}(s) = \tilde{F}_b(s) \quad . \tag{2}$$

These equations are diagonalized with the mass normalized eigenvectors Φ_b, such that $\Phi_b^T M_b \Phi_b = I$, $\Phi_b^T K_b \Phi_b = \Omega_b^2$ and $x = \Phi_b g$. Thus,

$$[s^2 I + \Omega_b^2]\tilde{g}(s) = \Phi_b^T \tilde{F}_b = \tilde{G}_b \quad . \tag{3}$$

There is a unique solution $\tilde{g}_b$ to this problem everywhere the left hand side is invertable. Note that functional dependence of $\tilde{g}$ and $\tilde{G}$ on s will be implied but left out from here on.

The optimization proceeds to a modified structural model with eigenvectors Φ_m, such that $\Phi_m^T M_m \Phi_m = I$, $\Phi_m^T K_m \Phi_m = \Omega_m^2$ and $x = \Phi_m g$ and finally to an expression similar to equation 3. From here on, a unified notation will be used in which the subscript γ is either b for baseline or m for modified model. With this notation, the aerodynamic forcing of the structure can be written

$$\tilde{F}_\gamma(s) = q_\infty H(s) \tilde{x}(s)_\gamma \quad \gamma = (b, m) \quad . \tag{4}$$

Since the AIC matrix $H(s)$ is node dependent only, and absent large geometric changes, the same nodal AIC matrix will apply to the baseline and modified structures [19, 32].

Write equation 4 in generalized coordinates

$$\tilde{G}_\gamma = \Phi_\gamma^T \tilde{F}_\gamma = q_\infty \Phi_\gamma^T H(s) \Phi_\gamma \tilde{g}_\gamma = q_\infty Q_\gamma(s) \tilde{g}_\gamma \tag{5}$$

where Q_γ is the gAIC matrix. A relationship between the gAIC of the baseline and modified structures is required. An orthogonal basis can be used such as that obtained by an application of the Gram-Schmidt procedure [35, 36] to the baseline modes. On the other hand, it is sometimes advantageous to use a nonorthogonal basis, for example, the use of linear normal modes as bases for a nonlinear structure [37–40]. In the present case, the modified structure mode shapes can be expressed in terms of the eigenvectors of the baseline undamped structure using

$$\Phi_\gamma = \Phi_b C_\gamma \quad . \tag{6}$$

C_γ is a matrix of constant coefficients where $C_b = I$ for the baseline structure and $C_m \neq I$ for the modified structure. See also equation 3 of Ref. 32. Substituting equation 6 into equation 5 yields

$$\tilde{G}_\gamma = q_\infty C_\gamma^T \Phi_b^T H \Phi_b C_\gamma \tilde{g}_\gamma = q_\infty C_\gamma^T Q_b C_\gamma \tilde{g}_\gamma \quad , \quad \gamma = (b, m) \quad , \tag{7}$$

which reveals that

$$Q_\gamma(s) = C_\gamma^T Q_b(s) C_\gamma \quad . \tag{8}$$

Equation 8 provides a means to calculate the gAIC of the modified structure from the baseline structure gAIC.

To calculate C, Ref. 32 starts from equation 6 and uses a least-squares solution given by

$$C_\gamma = (\Phi_b^T \Phi_b)^{-1} \Phi_b^T \Phi_\gamma \quad . \tag{9}$$

One can also compute the inverse of Φ_b if it is square, or pseudo-inverse otherwise, to get

$$C_\gamma = \Phi_b^{-1} \Phi_\gamma \quad . \tag{10}$$

An alternate approach is to use equation 6, the orthogonality of the baseline mode shapes with respect to the baseline mass matrix, and mass normalization of the baseline modal vectors to get

$$C_\gamma = \Phi_b^T M_b \Phi_\gamma \quad . \tag{11}$$

The most efficient method of computing C_γ can be determined on a case by case basis.

When performing CFD-based flutter or system identification, the mode shapes of the structure at structural nodes must be projected onto the surface of the CFD model. In this context, it is important to note that in each case the modal displacement at the structural model nodes are used in equations 9- 11 rather than that projected to the CFD surface. Thus, the modified mode shapes do not need to be projected onto the CFD surface and likewise a repeated

CFD analysis of the modified structure is not required. This simplification results in a significant reduction in the computation required.

For a complete baseline eigenvector basis, the representation of the modified modes will be exact. For a model with N degrees of freedom, but with only N_r modes retained (typically $N_r \ll N$), the modified modes calculated by equation 6 will be approximate. To improve the accuracy requires the use of an enriched basis set to calculate C_m. It is possible to get a reduced set of modes Φ_m that is exact by using all N basis vectors (Φ_b) in calculating the coefficient matrix C_m, which in this case will have dimensions $N \times N_r$. From a practical standpoint, a few additional modes used to calculate Q_m can result in increased accuracy. One can partition the baseline gAIC Q_b into an $N_r \times N_r$ submatrix designated by subcript rr and additional submatrices re, er and ee (ee submatrix having dimensions $(N_e - N_r) \times (N_e - N_r)$) to get

$$Q_b = \begin{bmatrix} (Q_b)_{rr} & (Q_b)_{er} \\ (Q_b)_{re} & (Q_b)_{ee} \end{bmatrix} \quad . \tag{12}$$

The addition of a few modes beyond N_r may result in somewhat better accuracy in the retained modes without a large increase in the system identification of the N_e mode responses. In this case C_m will have dimensions $N \times N_e$.

A way to assess the adequacy of the N_e modes is to do a cross correlation of the approximated modified modes (Φ_m^I) using equation 6 and the exact modified modes (Φ_m)

$$\beta = (\Phi_m^I \cdot \Phi_m) / (\Phi_m \cdot \Phi_m) \tag{13}$$

where an exact representation will give $\beta = 1$.

III. Flutter Equation and Optimization Method

The aerodynamic stiffness, damping, mass and wake induced lag effect are introduced by the Roger rational function approximation [34], which are transformed into the nondimensional Laplace variable $p = sL_R/U_\infty$

$$Q_b(p)\tilde{g} = [A_{0b} + pA_{1b} + p^2 A_{2b} + \sum_{n=1}^{N_{lags}} pA_{(n+2)_b}/(p - \lambda_n)]\tilde{g} \tag{14}$$

where N_{lags} is the number of lag states with root λ_n for lag n. These equations embody the unsteady aerodynamics which can be supplied by the DLM or URANS equations. The flutter equations (which now include a damping term) are written

$$[\frac{U_\infty^2}{L_R^2} M_\gamma p^2 + \frac{U_\infty}{L_R} D_\gamma p + \Omega_\gamma - \tilde{r}]\tilde{g} = 0 \tag{15}$$

where

$$\begin{aligned} M_\gamma &= I - q_\infty C_\gamma^T A_{2b} C_\gamma \quad , \quad D_\gamma = 2\zeta_\gamma \Omega_\gamma - q_\infty C_\gamma^T A_{1b} C_\gamma \\ K_\gamma &= \Omega_\gamma - q_\infty C_\gamma^T A_{0b} C_\gamma \quad , \quad \tilde{r} = q_\infty \sum_{n=1}^{N_{lags}} C_\gamma^T pA_{(n+2)_b} C_\gamma / (p - \lambda_n)] \quad . \end{aligned} \tag{16}$$

These equations are reformulated in state-space form, and the migration of the system's Laplacian eigenvalues, as a function of dynamic pressure q_∞ (or more commonly, equivalent air speed U_{EAS}), are simply computed with the p-method [41]. The Laplacian may be expanded as $p = \eta + i \cdot k$; an η value greater than zero indicates an unstable system, and η is equal to zero at the flutter point. Rather than actually locate these flutter points, a method more amenable to the gradient based optimization used here is discussed by Hajela [42] and Ringertz [18], where the traces

of η as a function of U_{EAS} must be below some bounding curve. This method allows the flutter mechanism to change identity during the optimization process, while still maintaining a smooth design space. Specifically:

$$\eta \leq \begin{cases} \eta^* \cdot (3 \cdot U^* \cdot U_{EAS}^2 - 2 \cdot U_{EAS}^3) / (U^*)^3 & 0 \leq U_{EAS} \leq U^* \\ c \cdot (U_{EAS} - U^*)^2 - \eta^* & U_{EAS} > U^* \end{cases} \tag{17}$$

where U^* is the minimum allowable flutter equivalent air speed, typically based on a 20% margin, η^* is the requisite damping at this flutter margin, and c is a quadratic scaling parameter. If η^* is set to 0, the method of Ringertz [18] is recovered. Critical U_{EAS} points (local minima) of the inequality in Eq. 17 are computed and lumped together into a single aggregate constraint via the Kreisselmeier-Steinhauser (KS) function [43].

For the gradient based optimization exercises discussed below, the derivative of critical points in Eq. 17 with respect to various structural sizing design variables must be computed analytically. The eigenvalue derivatives are simply computed using methods in Ref. 44 via a fixed-mode approximation, where the derivative of the mode shapes (Φ_m) with respect to design variables is neglected for the purposes of gradient computations.

During the optimization process (discussed in detail below), the numerical optimizer will continually update the structural details of the wing. At a given design iteration, the mode shapes of the current structure are designated Φ_m. The baseline mass matrix M_b, mode shapes Φ_b, and gAIC matrix Q_b are all constant and read from disk at the start of the procedure, and the procedures outlined above are used to compute the gAIC of the current structural iterate, Q_γ. The analytical derivatives of these baseline terms (M_b, Φ_b, Q_b) with respect to the modified structural layout design variables are exactly zero. Derivatives of Q_γ are approximated to be zero via the fixed-mode approximation discussed above.

IV. Results

As an example, consider the undeflected common research model (uCRM). The uCRM is a jig shape of the 1g wing shape model developed in Ref. 45. The uCRM is a generic transport configuration with a standard rib/spar wingbox. The layout of the rib/spar wingbox is shown in Figure 1. Figure 2 presents the DLM aerodynamic panels used in this study. This structure and aerodynamic panel layout has been used in previous static aeroelastic optimization studies [7]. This model and a version with a higher aspect ratio, is being analyzed by the NASA Performance Adaptive Aeroelastic Wing (PAAW) research project for a cruise condition at Mach 0.85. Dynamic aeroelastic optimization studies with the uCRM have been performed elsewhere, which included flutter optimization using DLM aerodynamics [24]. A similar optimization will be performed here, but with the URANS aerodynamics solved with the high-fidelity Navier-Stokes solver FUN3D v12.8. The Navier-Stokes code FUN3D (fully unstructured three-dimensional Navier-Stokes) is a finite volume unstructured CFD code for compressible flows [46, 47]. FUN3D solves the steady and unsteady Reynolds-averaged Navier-Stokes (URANS) flow equations loosely coupled with the Spalart-Allmaras turbulence model [48] on a tetrahedral mesh. The surface triangulation of this mesh is shown in Figure 3. System identification of the aerodynamic response to a perturbation of each mode is performed in the manner addressed in Ref. 33. The perturbation is a Gaussian pulse, which produces the generalized aerodynamic force response. A fast Fourier transform is applied to the time histories to produce the gAIC.

A. Retained and Exanded Mode Sets

Before discussing the flutter calculations, the influence of the number of modes in the expanded set in comparision to the retained number of modes will be investigated here. The cross correlation (Eq. 13) provides a metric to assess the adequacy of the expanded mode set chosen. The structural model has a complete set of 56242 nodes resulting in a large set of eigenvectors, whereas the expanded and retained mode sets are significantly smaller than this. Two

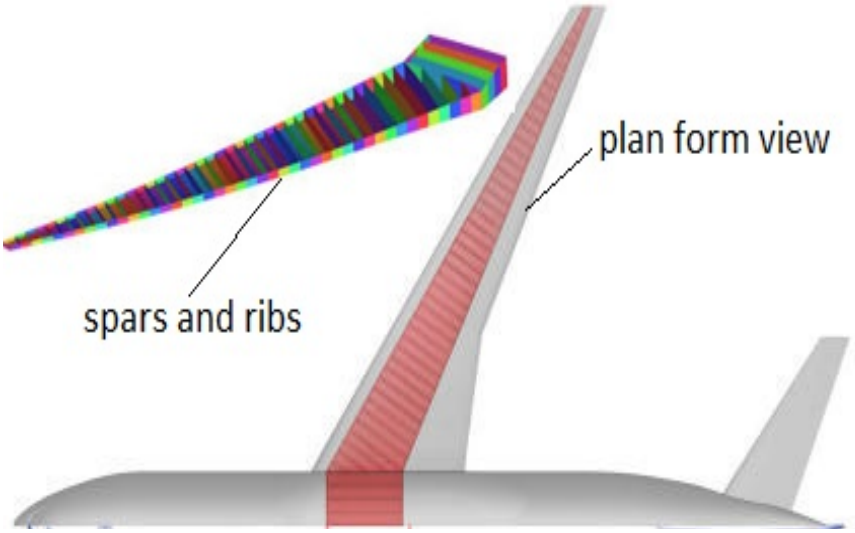

Fig. 1 uCRM wing-box structure from Ref. 7.

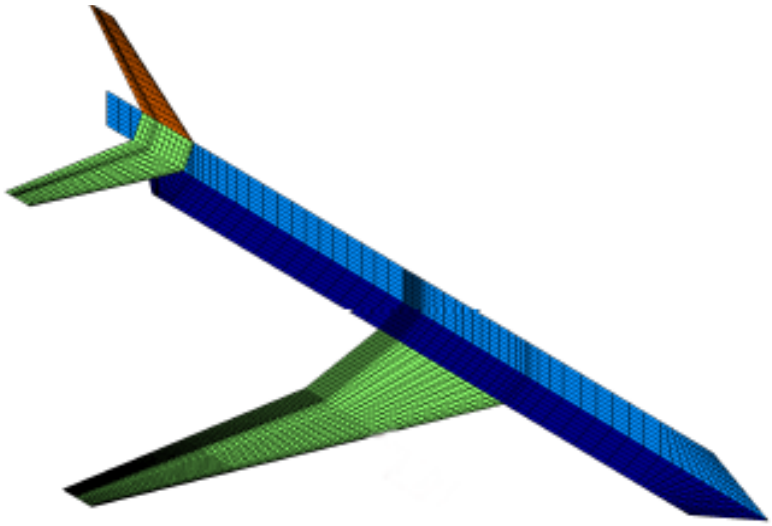

Fig. 2 uCRM DLM panels from Ref. 24.

sets of retained modes are constructed. One set has 20 retained modes (N_r = 20) and the other has 25 retained modes (N_r = 25). The first set (N_r = 20) is constructed using no expansion of the mode set, i.e. N_e = 20. The correlation measure is found in the second column of Table 1. The correlation measure for the case in which N_r = 25 while being constructed from a set with N_e = 100 is found in the third column of Table 1. The remaining column gives the correlation measure for N_r = 20 and N_e = 25. When N_r = N_e = 20, there is a marked drop off in the accuracy of the last 8-9 modes. Retaining a much larger expanded set (N_e = 100) results in much better accuracy in all the modes, while in the case in which N_r = 20 and N_e = 25, there is some improvement in all the modes, and especially in modes 15-20.

B. Flutter Onset

Since the target cruise condition is Mach 0.85, attention to potential nonlinear transonic effects such as shock motion and shock separation is important to identifying flutter onset. Transonic nonlinearity can reduce the flutter onset

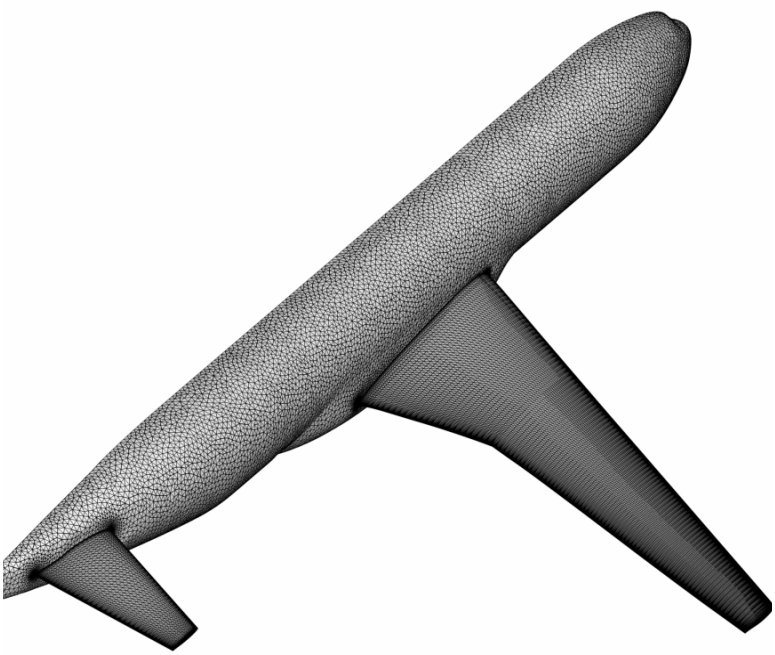

Fig. 3 uCRM surface mesh for URANS calculation.

dynamic pressure in a Mach range typically just below Mach 1. In the present configuration, nonlinear transonic effects are clearly evident at Mach 0.85. To see this effect, flutter simulations have been performed with DLM aerodynamics and URANS aerodynamics at Mach 0.70 and 0.85. The evolution of the modal flutter damping with increase in atmospheric density and speed are shown for the two Mach numbers in Figures 4 and 5.

Using DLM aerodynamics, the onset of instability is generally around the same density at Mach 0.70 and 0.85. Using a URANS analysis, however, the onset of aeroelastic instability is clearly much lower at Mach 0.85. The significant difference between flutter onset using DLM and URANS aerodynamic models at Mach 0.85 motivates the present work. URANS flutter calculations using the method outlined in Sec. II will accurately provide flutter onset, while the approach of Sec. III will be used to optimize the structure under the flutter onset constraint.

C. Approximating the Flutter Onset of a Modified Structural Model Using Baseline DLM and URANS Aerodynamics

To verify the performance of the method, the flutter onset of the baseline and modified finite element structural models will be compared. The gAIC matrix of the modified structure is calculated using the baseline and modified structural models and the URANS Q_b. The aerodynamics are implemented into the flutter equations using a Roger approximation. Figure 6 shows the damping for the baseline and the modified models using URANS aerodynamics. These two models are sufficiently different to provide a realistic assessment of the current capability.

The first step is to verify the model. The flutter onset for this configuration is a coalescing of the first three modes. Since these modes are the most significant, and differ most from the baseline to modified model, the gAIC matrix terms for the 1^{st} two of these modes will be scrutinized. All the remaining results in this paper use $N_r = N_e = 20$. Figures 7 and 8 show four of the gAIC terms, each of which involves the second mode interacting with itself or one of the other first three modes. Figure 7 is derived from the DLM theory. Figure 8 is derived from URANS theory. For these gAIC terms, the baseline and modified models are easily differentiated. It is clear that the modified aerodynamic model using the method of Sec. II and that directly from the modified models are identical. This is true using either the DLM or the URANS theory.

Table 1 β (Equation 13).

mode number	N_r = 20 N_e = 20	N_r = 25 N_e = 100	N_r = 20 N_e = 25
1	0.99999	1.00000	1.00000
2	0.99833	0.99959	0.99931
3	1.00023	1.00004	1.00010
4	1.00034	1.00031	1.00030
5	1.00042	0.99950	0.99981
6	1.00090	0.99955	1.00020
7	1.00112	1.00134	1.00130
8	0.99985	0.99984	0.99999
9	1.00092	0.99983	1.00110
10	0.99860	1.00088	1.00130
11	0.99011	1.00002	0.99881
12	0.98912	0.99985	1.00320
13	0.99092	1.00041	0.99945
14	0.98693	0.99883	1.00030
15	0.97804	0.99890	0.99302
16	0.98685	0.99814	0.99912
17	0.91360	0.99384	0.99718
18	0.95756	0.99620	0.99481
19	0.97184	0.99208	0.97882
20	0.96091	1.00027	0.97577
21	—	0.97525	—
22	—	0.99766	—
23	—	0.93356	—
24	—	1.00524	—
25	—	1.00055	—

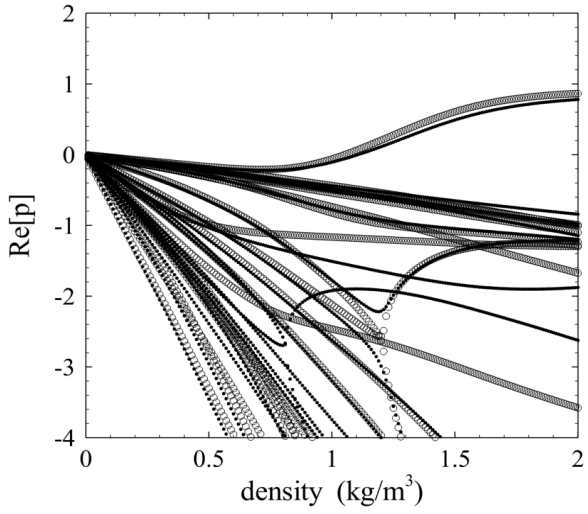

Fig. 4 Flutter damping versus density for the baseline model using DLM and URANS aerodynamics, Mach 0.70**,**
(◯ DLM, • URANS).

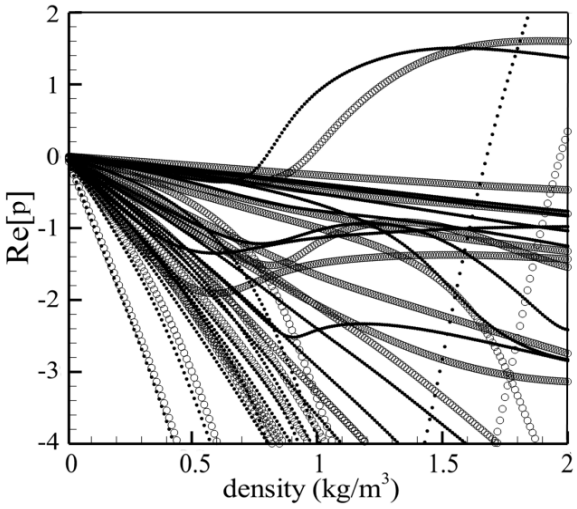

Fig. 5 Flutter damping versus density for the baseline model using DLM and URANS aerodynamics, Mach 0.85**, (◯ DLM, • URANS).**

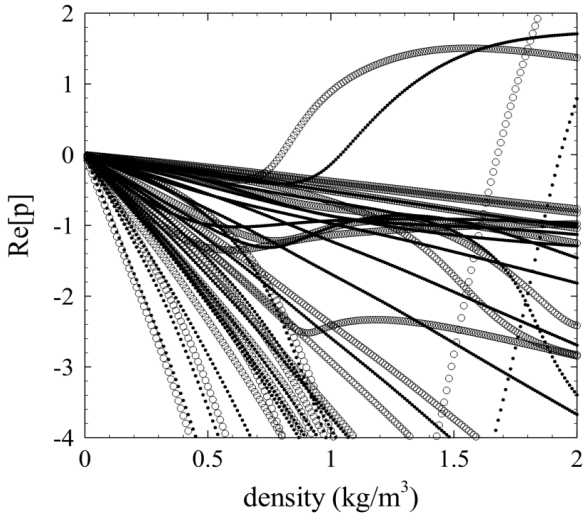

Fig. 6 Flutter damping versus density using URANS aerodynamics, Mach 0.85**, (• modified, ◯ baseline).**

Figure 9 compares the evolution of the flutter damping for the URANS modified model using the method of Sec. II and that computed directly from a gAIC matrix calculated by a URANS system identification of the modified modes. Except for slight differences in some of the higher frequency modes, the two models are identical. The differences in the higher frequency modes are most likely due to a drop off in accuracy given that $N_e = N_r$.

Finally, a comparision is shown in Figure 10 between the flutter damping calculated using the URANS baseline model, the URANS model created using the method of Sec. II, and damping calculated from a time-marching URANS flutter simulation. The damping of the time marching flutter solutions is obtained from the modal time histories by the log decrement method and flutter frequency by the spacing of zero crossings. The URANS time-marching flutter

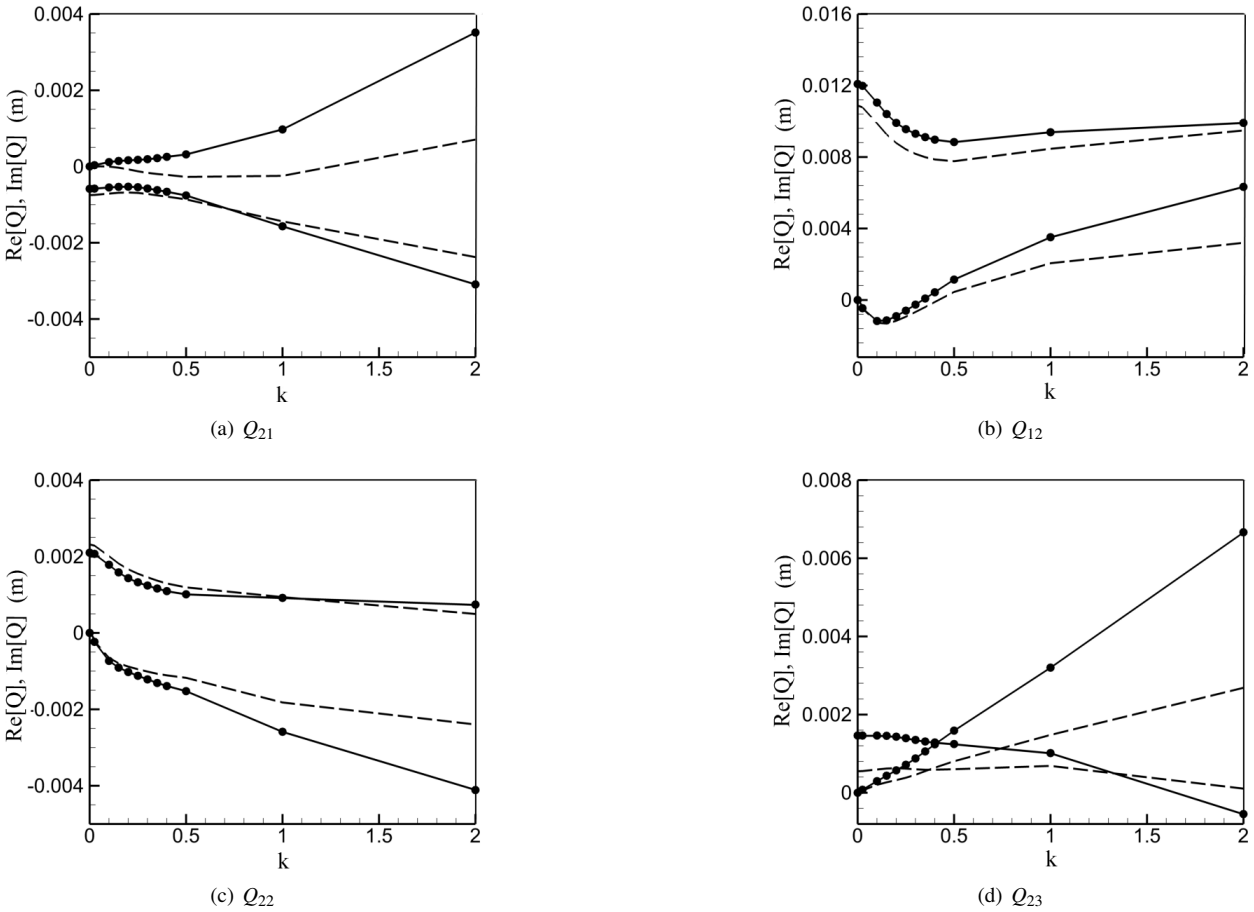

(a) Q_{21} (b) Q_{12}

(c) Q_{22} (d) Q_{23}

Fig. 7 DLM gAIC terms, (– – – baseline, – modified, ● modified using equations 8 and 11).

simulation is started from a static aeroelastic solution at a slightly negative angle of attack in order to approximate a zero-lift condition. The URANS time-marching flutter simulation also includes wing weight while the URANS system identification solution did not include wing weight and is also started from an undeformed vehicle shape. Furthermore, the initial modal velocity used to start the time-marching flutter solutions was somewhat larger than the excitation used to create the analytical aerodynamic models. Because of these differences in the way damping and flutter frequencies are obtained, some differences are to be expected between the time-marching flutter and the frequency domain solutions. The time-marching solution damping $(Re[p])$ is calculated from the true damping (ζ) and the flutter frequency (ω_f) at two dynamic pressures near the flutter onset predicted by the present theory for both the baseline and the modified models. The damping calculated from the time-marching solutions is about a percent below the predicted flutter onset point in either case. On the other hand, the slope of the damping near flutter onset, and the increment in flutter onset from the baseline to modified solutions is well simulated by the present method.

D. Optimization Results

The optimization problem considered here seeks to find the structural sizing layout of the wingbox, which minimizes the structural mass while still satisfying several constraints on aeroelastic performance. Design variables are based on the patch-level discretization in Fig. 1, where each skin panel is a design patch, each rib is a patch, and each spar section is a patch. Design variables include the shell thickness of each patch (bounded between 3 and 30 mm), the thickness of the stiffeners attached to each patch (bounded between 2.5 and 30 mm), and the height of the

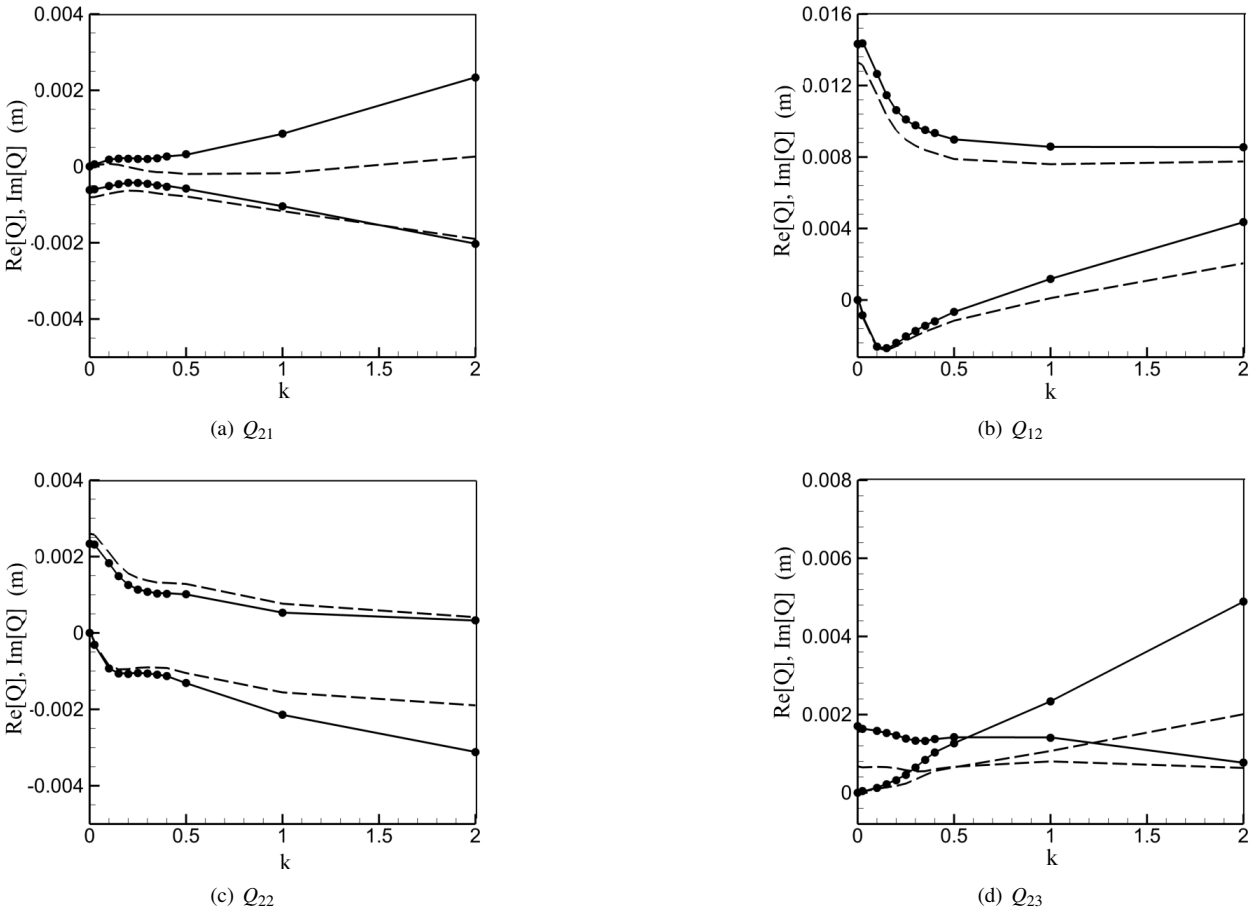

(a) Q_{21} (b) Q_{12}

(c) Q_{22} (d) Q_{23}

Fig. 8 URANS gAIC terms, (– – – baseline,– modified, ● modified using equations 8 and 11).

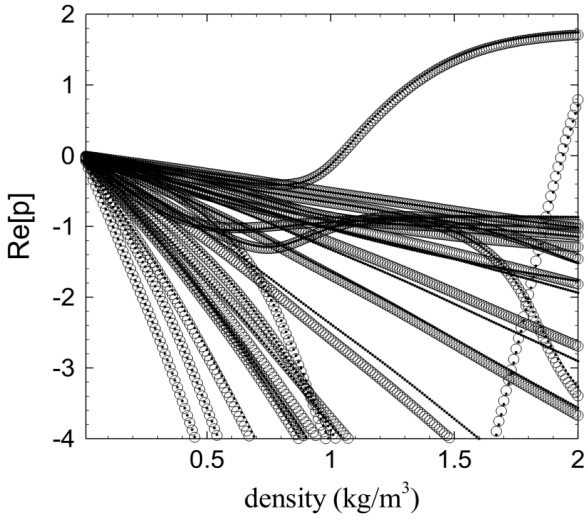

Fig. 9 Flutter damping versus density from URANS aero, Mach 0.85, generated with modified structure modes (•) and URANS transformed aero using equation 8 (◯).

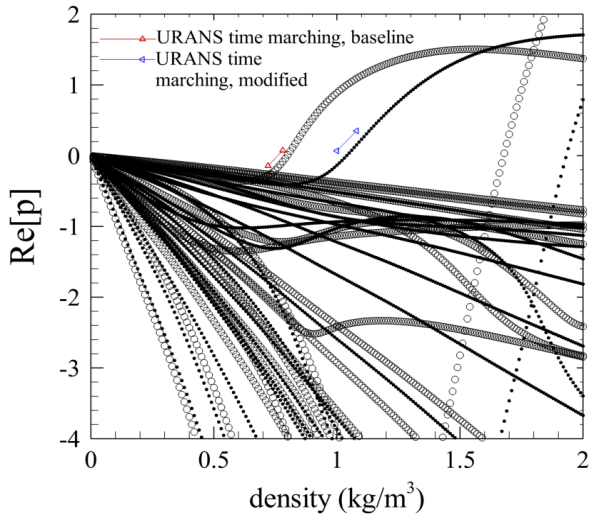

Fig. 10 Flutter damping versus density, comparing analytical with time-marching URANS.

stiffeners attached to each patch (bounded between 30 and 150 mm). The stiffeners are modeled as smeared T-shaped stiffeners [49], where the flange is bonded to the shell members. The total number of design patches is 237, and the total number of design variables is 711.

The objective function is the structural mass, computed by the volume of the wingbox finite element model. This function is minimized subject to many constraints. First, a flutter constraint is enforced at a Mach number of 0.85, across a range of flutter margins, using the methods outlined in Sec.s II and III. A series of static aeroelastic constraints are also enforced, spread across four trimmed maneuver loads: a 2.5g pull-up, a -1g push-over, a roll maneuver, and a 2g landing load. All cases are run at the aircraft dive speed at sea level with full fuel. For each load case, the stresses in each finite element are computed, and the KS function is used to compress all of the elemental failure function values within a given patch into a single metric.

Next, buckling analyses are run for each stiffened panel in the upper and lower skins using a Rayleigh-Ritz method (assumed buckling modes). Both global buckling of a stiffened panel (bordered by ribs and spars) and local buckling between each stiffener is computed, where simply-supported boundary conditions are used for both scenarios. As with the stress metrics, each buckling eigenvalue for a given stiffened panel is compressed into a single KS function. Design constraints are placed on both the stress and the buckling KS functions. The final gradient-based optimization problem is solved with the Globally-Convergent Method of Moving Asymptotes tool [50].

The optimal structural mass, as a function of the flutter margin constraint boundary (using a dive speed of 185 m/s), is shown in Fig. 11, for two cases. The first case uses URANS to compute the baseline gAICs Q_b, whereas the second case uses linear DLM aerodynamics. Both sets of results then use the transformation methods detailed above, to compute Q_γ as the structure is optimized. For low flutter margins in Fig. 11, the flutter constraint is very easy to satisfy, and is inactive (i.e., the static aeroelastic constraints drive the design process entirely). The structural mass (objective function) in this case is 8,631 kg. Increasing the flutter margin makes the constraint harder to satisfy, resulting in an increase in the structural mass. As also seen in the figure, the URANS model predicts a more aggressive flutter mechanism than the linear DLM model and therefore, results in heavier structural models. This added weight is due to the fact that the DLM does not accurately predict the drop in the flutter onset dynamic pressure typically seen in the transonic Mach range, frequently called the transonic dip. At a margin of 1.2, the URANS flutter model is 4.3% heavier.

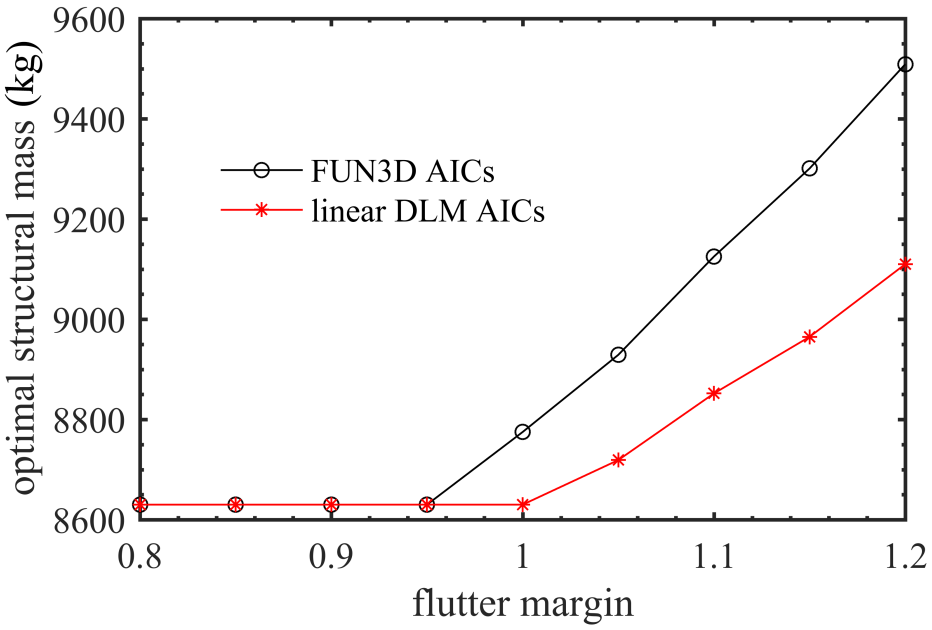

Fig. 11 Optimal structural mass for various flutter constraint boundaries.

The equivalent skin thickness distributions (sum of the panel thickness and the smeared stiffener thickness) are shown in Fig. 12, for three cases: the design with an inactive flutter constraint, and the two designs (URANS and DLM) with a 1.2 flutter margin constraint. For all cases, peak thickness tends to occur between the wing root (span location of 3 m) and the Yehudi break in the trailing edge (span location of 10 m), and then trends toward minimum gage at the wingtip. The addition of the flutter constraint increases the thicknesses in various areas, as expected, but the redistribution of material is quite different for the two flutter models. Particularly in the lower skin, the URANS model forces an increase in thickness localized near span location of 10 m, whereas the DLM model shows more of a global thickness increase across most of the skin. Such a result indicates that while the two aerodynamic models are both linearizations (in the case of DLM, the linearization is about the null state), and the flutter-damping plots presented above look topologically similar, the two flutter models in fact rely on inherently different flutter mechanisms, and therefore force the optimizer to react in fairly different ways. Neither model, it should be noted, is able to account for changes in the underlying shock structure with changes in the structural sizing variables, as the URANS linearization is conducted just once, and the resulting Q_b matrix projected from one modal space to the next.

V. Concluding Remarks

A concise transformation of the unsteady generalized aerodynamic influence coefficient matrix based on the baseline structural modes is used to optimize a transport wingbox model under a transonic flutter constraint (among other linear static aeroelastic constraints), where the flutter constraint boundaries are computed using unsteady high-fidelity Reynolds-averaged Navier-Stokes aerodynamic model. Rather than recomputing a complete CFD-based time-marching flutter solution at each design iteration, the approach requires only a single matrix transformation. System identification techniques are used to extract linearized generalized aerodynamic influence coefficients for a baseline wing configuration. An inexpensive modal projection method is then used to transform these baseline aerodynamic terms into the modal space inhabited by the various structural iterates obtained during the optimization process.

The results demonstrate the need for transonic flutter computations, versus purely-linear physics, and then demonstrate the accuracy and the efficiency of both the system identification techniques, and the modal projection techniques.

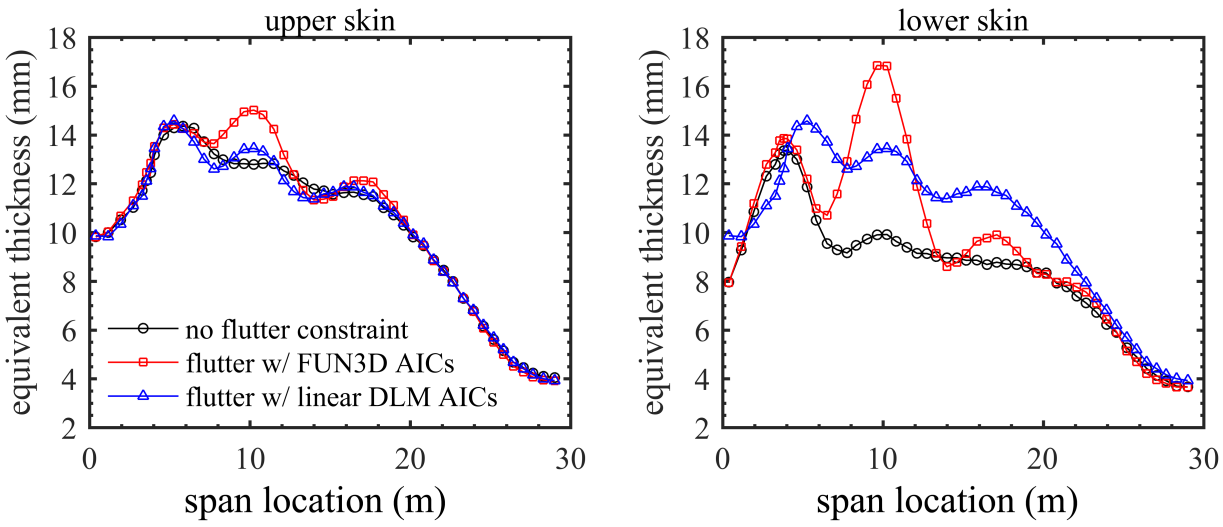

Fig. 12 Upper and lower skin equivalent thickness distributions.

Finally, a structural optimization is presented with a large number of structural sizing design variables, which seeks to minimize structural mass under static aeroelastic stress and buckling constraints, as well as a flutter constraint. Optimization results are presented for a large range of required flutter margins, using both a CFD-based flutter constraint, and an entirely linear DLM-based flutter constraint. The CFD model predicts a more aggressive flutter mechanism than the linear DLM model (as the latter does not capture the flutter dip), and results in a heavier optimal structure. Furthermore, the optimal distribution of material under the flutter constraint identified by optimizing the structural models coupled with URANS and DLM aerodynamics is highly dissimilar.

Acknowledgement

The authors wish to acknowledge Steven Massey for creating the uCRM CFD mesh. This work was supported by the NASA performance adaptive aeroelastic wing (PAAW) and the transonic truss-braced wing (TTBW) projects.

References

[1] Niu, M., *Airframe Structural Design*, Cnmilit Press Ltd., 1988.

[2] Bendiksen, O., "Review of Unsteady Transonic Aerodynamics," *Progress in Aerospace Sciences*, Vol. 47, 2011, pp. 135–167.

[3] Martins, J. R. R. A., Alonso, J. J., and Reuther, J. J., "High-Fidelity Aero-Structural Design Optimization of a Supersonic Business Jet," *Journal of Aircraft*, Vol. 41, No. 3, 2004, pp. 523–530.

[4] Chittick, I. R. and Martins, J. R. R. A., "An Asymmetric Suboptimization Approach to Aerostructural Optimization," *Optimization and Engineering*, Vol. 10, No. 1, 2009, pp. 133–152.

[5] Martins, J. R. R. A., Alonso, J. J., and Reuther, J. J., "A Coupled-Adjoint Sensitivity Analysis Method for High-Fidelity Aero-Structural Design," *Optimization and Engineering*, Vol. 6, No. 1, 2005, pp. 33–62.

[6] Kenway, G. K. W., Kennedy, G. J., and Martins, J. R. R. A., "A Scalable Parallel Approach for High-Fidelity Steady-State Aeroelastic Analysis Computations Derivative Computations," *AIAA Journal*, Vol. 52, No. 5, 2014, pp. 935–951.

[7] Kenway, G., Martins, G., and Kennedy, G., "Aerostructural Optimization of the Common Research Model Configuration," *AIAA Aviation Conference*, American Institute of Aeronautics and Astronautics, Atlanta, GA, June 16-20 2014.

[8] Barcelos, M., Bavestrello, H., and Maute, K., "A Schur-Newton-Krylov Solver for Steady-State Aeroelastic Analysis and Design Sensitivity Analysis," *Computer Methods in Applied Mechanics and Engineering*, Vol. 195, No. 17-18, 2006, pp. 2050–2069.

[9] Barcelos, M. and Maute, K., "Aeroelastic Design Optimization for Laminar and Turbulent Flows," *Computer Methods in Applied Mechanics and Engineering*, Vol. 197, No. 19-20, 2008, pp. 1813–1832.

[10] Liem, R. P., Kenway, G. K., and Martins, J. R. R. A., "Multi-Point, Multi-Mission, High-Fidelity Aerostructural Optimization of a LongRange Aircraft Configuration," *12th AIAA Aviation Technology, Integration, and Operations (ATIO) Conference and 14th AIAA/ISSM*, No. AIAA 2012-5706, Indianapolis, IN, September 17-19 2012.

[11] Morris, A. M., Allen, C. B., and Rendall, T. C. S., "Wing Design by Aerodynamic and Aeroelastic Shape Optimisation," *26th AIAA Applied Aerodynamics Conference*, No. AIAA 2008-7054, Honolulu, Hawaii, August 18-21 2008.

[12] Thomas, J. P., Dowell, E. H., and Hall, K. C., "Discrete Adjoint Method for Nonlinear Aeroelastic Sensitivities for Compressible and Viscous Flows," *Structures, Structural Dynamics, and Materials and Co-located Conferences*, No. AIAA 2013-1860, Boston, MA, April 8-11 2013.

[13] Thomas, J. P. and Dowell, E. H., "Discrete Adjoint Approach for Aeroelastic Design Optimization," *AIAA Aviation Forum*, No. AIAA 2014-2298, Atlanta, GA, June 16-20 2014.

[14] Mani, K. and Mavriplis, D., "Adjoint-Based Sensitivity Formulation for Fully Coupled Unsteady Aeroelasticity Problems," *AIAA Journal*, Vol. 47, No. 8, 2008, pp. 1902–1915.

[15] Economon, T. D., Palacios, F., and Alonso, J. J., "Unsteady Continuous Adjoint Approach for Aerodynamic Design on Dynamic Meshes," *AIAA Journal*, Vol. 53, No. 9, 2015, pp. 2437–2453.

[16] Nadarajah, S. K., McMullen, M., and Jameson, A., "Non-Linear Frequency Domain Based Optimum Shape Design for Unsteady ThreeDimensional Flow," *44th AIAA Aerospace Sciences Meeting and Exhibit*, No. AIAA 2006-1052, Reno, NV, January 9-12 2006.

[17] Rudisill, C. S. and Bhatia, K. G., "Optimization of Complex Structures to Satisfy Flutter Requirements," *AIAA Journal*, Vol. 9, No. 8, 1971, pp. 1487–1491.

[18] Ringertz, U. T., "On structural optimization with aeroelasticity constraints," *Structural Optimization*, Vol. 8, 1994, pp. 16–23.

[19] Haftka, R. T. and Yates, E. C., "Repetitive Flutter Calculations in Structural Design," *Journal of Aircraft*, Vol. 13, No. 7, July 1976, pp. 454–461.

[20] Crema, L. B., Mastroddi, F., and Coppotelli, G., "Aeroelastic Sensitivity Analyses for Flutter Speed and Gust Response," *Journal of Aircraft*, Vol. 37, No. 1, 2000, pp. 172–180.

[21] van Keulen, F., Haftka, R. T., and Kim, N. H., "Review of options for structural design sensitivity analysis. Part 1: Linear systems," *Computational Methods in Applied Mechanical Engineering*, Vol. 294, 2005, pp. 3213–3243.

[22] Stanford, B. K., "Role of Unsteady Aerodynamics During Aeroelastic Optimization," *AIAA Journal*, Vol. 53, No. 12, 2015, pp. 3826–3831.

[23] Stanford, B. K., Stanford, C. D., and Jutte, C. V., "Aeroelastic Tailoring of Transport Wings Including Transonic Flutter Constraints," *AIAA SciTech*, No. AIAA 2015-1127, Kissimmee, Florida, January 5-9 2015.

[24] Stanford, B. K., "Static and Dynamic Aeroelastic-Tailoring with Variable Camber Control," *15th AIAA Dynamics Specialists Conference*, No. 2016-1097, San Diego, CA, January 4-8 2016 2016.

[25] Vio, G. A. and Cooper, J. E., "Optimisation of Composite Structures for Aeroelastic Applications using Evolutionary Algorithms," *49th AIAA/ASME/ASCE/AHS/ASC Structures, Structural Dynamics, and Materials Conference*, No. AIAA 2008-1972, Schaumburg, IL, April 7-10 2008.

[26] Stodieck, O., Cooper, J. E., Weaver, P. M., and Kealy, P., "Optimisation of Tow-Steered Composite Wing Laminates for Aeroelastic Tailoring," *55th AIAA/ASME/ASCE/AHS/ASC Structures, Structural Dynamics, and Materials Conference*, No. AIAA 2014-0343, National Harbor, Maryland, January 13-17 2014.

[27] Yurkovich, R., "Status of Unsteady Aerodynamic Prediction for Flutter of High-Performance Aircraft," *Journal of Aircraft*, Vol. 40, No. 5, 2003, pp. 832–842.

[28] Neill, D., Johnson, E., and Canfield, R., "ASTROS: A Multidisciplinary Automated Structural Design Tool," *Journal of Aircraft*, Vol. 27, No. 12, 1990, pp. 1021–1027.

[29] Dodd, A., Kadrinka, K., Loikkanen, M., Rommel, B., Sikes, G., Strong, R., and Tzong, T., "Aeroelastic Design Optimization Program," *Journal of Aircraft*, Vol. 27, No. 12, 1990, pp. 1028–1036.

[30] Palacios, R., Climent, H., Karlsson, A., and Winzell, B., "Assessment of Strategies for Correcting Linear Unsteady Aerodynamics using CFD to Test Results," *International Forum on Aeroelasticity and Structural Dynamics*, Madrid, Spain, June

12-15 2011.

[31] Chen, P., Gao, X., and Tang, L., "Overset Field-Panel Method for Unsteady Transonic Aerodynamic Influence Coefficient Matrix Generation," *AIAA Journal*, Vol. 42, No. 9, 2004, pp. 1775–1787.

[32] Chen, P. C., Sarhaddi, D., and Liu, D. D., "Transonic-Aerodynamic-Influence-Coefficient Approach for Aeroelastic and MDO Applications," *Journal of Aircraft*, Vol. 37, No. 1, January 2000, pp. 85–94.

[33] Bartels, R. E., "Flexible Launch Vehicle Stability Analysis Using Steady and Unsteady Computational Fluid Dynamics," *Journal of Spacecraft and Rockets*, Vol. 49, No. 4, 2012, pp. 644–650.

[34] Roger, K. L., "Airplane Math Modeling Methods for Active Control Design," *AGARD-CP-228 Structural Aspects of Active Controls*, August 1977.

[35] Northington, J. S., "Basis Vector Quantification of Flutter Analysis Structural Modes," *Journal of Aircraft*, Vol. 46, No. 6, November-December 2009, pp. 2107–2114.

[36] Denegri, C. M., "Simple Quantitative Method to Compare Aircraft Wing Mode Shapes," *Journal of Aircraft*, Vol. 46, No. 3, May-June 2009, pp. 1082–1085.

[37] Guo, X. and Mei, C., "Using Aeroelastic Modes for Nonlinear Panel Flutter at Arbitrary Supersonic Yawed Angle," *AIAA Journal*, Vol. 41, No. 2, February 2003, pp. 272–279.

[38] Guo, X. and Przekop, A., "Energy-Based Modal Basis Selection Procedure for Reduced-Order Nonlinear Simulation," *51st AIAA/ASME/ASCE/AHS/ASC Structures, Structural Dynamics, and Materials Conference*, No. AIAA 2010-2796, Orlando, Florida, April 12-15 2010.

[39] Wang, Z., Liu, D. D., Chen, P. C., Yang, S., Zhang, Z., Mignolet, M. P., and Wang, X. Q., "An Expendient Aeroelastic ROM-ROM Methodology For Nonlinear Aerodynamic-Nonlinear Structural Interactions," *International Forum of Aeroelasticity and Structural Dynamics*, No. IFASD-2009-010, 2009.

[40] Przekop, A. and Rizzi, S. A., "Nonlinear Reduced-Order Random Response Analysis of Structures with Shallow Curvature," *AIAA Journal*, Vol. 44, No. 8, August 2006, pp. 1767–1778.

[41] Bisplinghoff, R., Ashley, H., and Halfman, R., *Aeroelasticity*, Addison-Wesley, 1955.

[42] Hajela, P., "A Root Locus-Based Flutter Synthesis Procedure," *Journal of Aircraft*, Vol. 20, No. 12, 1983, pp. 1021–1027.

[43] Kreisselmeier, G. and Steinhauser, R., "Systematic Control Design by Optimizing a Vector Performance Index," *International Federation of Active Controls Symposium on Computer-Aided Design of Control Systems*, Zurich, Switzerland, 1979.

[44] Adelman, H. and Haftka, R., "Sensitivity Analysis of Discrete Structural Systems," *AIAA Journal*, Vol. 24, No. 5, 1986, pp. 823–832.

[45] Vassberg, J., DeHaan, M., Rivers, S., and Wahls, R., "Development of a Common Research Model for Applied CFD Validation Studies," *AIAA Applied Aerodynamics Conference*, American Institute of Aeronautics and Astronautics, Honolulu, Hawaii, August 10-13 2008.

[46] Anderson, W. K. and Bonhaus, D. L., "An Implicit Upwind Algorithm for Computing Turbulent Flows on Unstructured Grids," *Computers and Fluids*, Vol. 23, No. 1, 1994, pp. 1–22.

[47] "FUN3D Manual," 2015.

[48] Spalart, P. R. and Allmaras, S. R., "One-Equation Turbulence Model for Aerodynamic Flows," *30th AIAA Aerospace Sciences Meeting and Exhibit*, No. 92-439, Reno, NV, January 6-9 1992.

[49] Stroud, W. and Agranoff, N., "Minimum-Mass Design of Filamentary Composite PPanel under Combined Loads: Design Procedure Based on Simplified Buckling Equations," Tech. Rep. TN D-8257, NASA, 1976.

[50] Svanberg, K., "A Class of Globally Convergent Optimization Methods Based on Conservative Convex Separable Approximations," *SIAM Journal of Optimization*, Vol. 12, 2002, pp. 555–573.